Materials Advances

ROYAL SOCIETY OF CHEMISTRY

PAPER

View Article Online
View Journal | View Issue

Cite this: *Mater. Adv.*, 2024, 5, 2012

Trimetallic MOF1@MOF2 heterostructure derived Co–NC@CuM–C for enhanced photothermal catalysis in styrene epoxidation†

Xinliu Zhao, Fusheng Liu, Yu-Zhen Chen * and Zhibo Li *

Constructing hierarchical MOF1-on-MOF2 composites using different binary MOFs is a promising strategy to develop multifunctional MOF precursors and their derivatives. However, the orientated growth of the heteroid MOF shell requires overcoming the mismatched cell lattices. Therefore, the desired assembly of MOF1@MOF2 with regular morphologies and sizes remains a significant challenge. Herein, a novel tri-metallic BMZIF@HKUST-1 with good dodecahedral morphology was successfully fabricated and pyrolyzed to obtain porous Co–NC@Cu–C, in which Cu and Co species were highly dispersed in the carbon skeleton and no agminated metal particles were observed. Interestingly, the carbon materials exert a good photothermal effect and can raise the system temperature from 25 to ~50 °C under visible light irradiation. In addition, a metal ion redox exchange strategy was adopted to avoid run-off of unstable Cu species in Co–NC@Cu–C during catalysis under harsh conditions. The optimal Co–NC@CuOPd–C achieved excellent activity (99%) and high selectivity (92.9%) in styrene epoxidation by photothermal catalysis benefitting from its multiple active sites and highest stability. The novel synthetic strategy can be further extended to more MOF types and provides plentiful metal sites for producing various fine chemicals.

Received 19th November 2023,
Accepted 5th January 2024

DOI: 10.1039/d3ma01024d

rsc.li/materials-advances

1 Introduction

The catalytic epoxidation of styrene to produce styrene oxide (SO) has attracted considerable attention because SO is an essential raw material for industrial synthesis of spices, pesticides and pharmaceuticals.[1–5] Of these, spice intermediates account for 90.78% of the total SO volume utilized. The global market size for styrene oxide was $70.0 million in 2021, with estimates surpassing $109 million in 2028.[6] Therefore, it is urgent to produce industrially SO with good yield and high purity. Three crucial factors, namely, catalyst, oxidant, and reaction temperature, significantly influence the styrene epoxidation efficiency. Generally, noble-metal-based catalysts like Ag, Pt, and Au show superb catalytic activity toward styrene epoxidation;[7–9] however, SO selectivity above 90% remains a great challenge.[10,11] Traditional oxidants such as organic peracids, $KMnO_4$ and chlorohydrin are usually added to help achieve good activity.[12–14] But the large amount of chemical waste produced has caused a serious pollution.[15,16] From economical, green, and long-life vantage points, molecular oxygen as an oxidant has been the optimal choice. For example, Fe_2O_3@mSiO_2-SH–Au gave a 65% conversion with 58% SO selectivity using O_2 as the oxidant.[17] Au/TiO_2-EC afforded a 56% conversion, yet only 17.5% SO selectivity.[18] Compared to precious metal catalysts, low-cost cobalt and copper species are also active toward styrene epoxidation.[19–21] Especially, copper species (Cu, Cu_xO) can activate molecular O_2 and enhance effectively the SO selectivity. Unfortunately, unstable copper species are readily oxidized and then leaching into some solvents. For example, as the most commonly used solvent for styrene epoxidation, acetonitrile readily coordinates with copper. Therefore, designing a method to stabilize Cu species in Cu-based catalysts would be more significant for good cost-efficiency and high SO selectivity.

Porous materials have been commonly utilized as supports to stabilize small metal NPs. Typically, metal–organic frameworks (MOFs) are well-known crystalline porous materials, constructed *via* organic ligands with metal ions (or clusters).[22–29] MOFs have been applied extensively in various fields such as heterogeneous catalysis,[30–32] drug delivery and imaging,[33,34] sensors,[35,36] and gas adsorption/separation.[37–40] More recently, MOFs served as excellent precursors or templates for the fabrication of various carbon-based materials and porous metals or metallic oxides.[41–48] These hybrid materials provided more possibilities in electrochemical reactions and heterogeneous catalysis.[49,50] Nonetheless, monometallic MOFs are subject to

College of Chemical Engineering, Qingdao University of Science and Technology, Qingdao 266042, Shandong, P. R. China

† Electronic supplementary information (ESI) available. See DOI: https://doi.org/10.1039/d3ma01024d

the limited metals in the periodic table, which hampers their utility, such as the Cu-MOF (HKUST-1) and Co-MOF (ZIF-67).[51] To enrich the metal sites, isostructural MOF-on-MOF materials (with the same ligand) have been developed,[52–58] and they include ZIF-67@ZIF-8, Fe-MIL-88B@Fe-MIL-88C, and UiO-67@UiO-66. In particular, the conjugation of two or more isomerous MOFs with different metals and ligands yields greater structural flexibility and more active species. For instance, HKUST-1-on-ZIF can provide both Cu and Co active sites, but such assembly is very challenging due to their unmatched cell lattices. Currently, similar assembly architectures like core–shell, hollow multi-shell and film-on-film MOFs (*e.g.*, UiO-66@ZIF-8, MIL-88B@ZIF-8, PCN-222@NU-1000, MIL-125@ZIF-67) and ternary MOF-on-MOF hybrids (*e.g.*, MIL-125@ZIF-67@ZIF-8) have been designed for various applications since 2009.[59–63] Anisotropic growth often results in abnormal morphology or poor assembly of the final composite (like sandwich-type hybrid MOFs and In-MIL-88B/Fe-MIL-88B/In-MIL-88B).[64] Research findings indicate that the morphology of MOFs and MOF derived materials may impact directly the intrinsic properties and their catalytic performance.[65] Furthermore, the well-defined crystalline structures of core–shell MOFs could help the establishment of the structure–activity relationship. To date, directional growth of the guest HKUST-1 on the host ZIF with well-matched cell lattices and regular morphology has not been studied.

Herein, two different MOFs (BMZIF (ZnCo-ZIF) and HKUST-1 (Cu-MOF)) with distinct crystal structures and morphologies were directionally assembled. The dodecahedral BMZIF core provided active Co sites,[66] and the HKUST-1 shell afforded Cu species to improve SO selectivity. This core–shell hierarchical BMZIF@HKUST-1, namely, HKZIF, is fleetly *in situ* reduced through procedural calcination under 20% H_2/Ar to obtain a porous core–shell Co–NC@Cu–C. Due to rapid reduction, no distinct Co and Cu NPs were observed; they were uniformly dispersed throughout the core or shell carbon framework. Copper readily oxidizes in an oxidizing atmosphere and washes into solution. To stabilize and preserve the copper sites, a metal ion (M^{n+}, M = Ag, Pt, Pd) exchange based on a spontaneous redox reaction yielded Co–NC@CuAg–C, Co–NC@CuOPd–C and Co–NC@Cu_2OPt–C (Scheme 1). Among them, Co–NC@CuOPd–C showed excellent catalytic activity (99% conversion and 92.9% selectivity) and high stability for styrene epoxidation using O_2 by photothermal catalysis. The trimetallic isostructural MOFs and the intricate metal ion exchange will open up novel pathways toward the rational design of MOF-based multifunctional catalysts for more widespread applications.

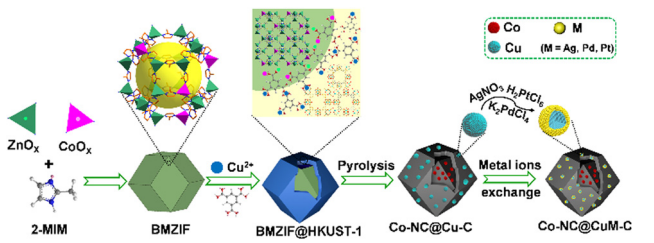

Scheme 1 Schematic illustration of the synthesis of isomerous BMZIF@HKUST-1, porous Co–NC@Cu–C and Co–NC@CuM–C.

2 Results and discussion

Cobalt species are active in oxidation reactions and copper species generally improve the chemoselectivity, so we selected the Co-ZIF and HKUST-1 (Cu-MOF) as MOF precursors. Given the presence of Zn could improve the surface area and porosity of the final porous carbon, Co-ZIF-67 was replaced by the ZnCo-BMZIF. The BMZIF and HKUST-1 are two completely different MOFs in terms of metal species, ligands, crystal structures, morphologies and properties. Therefore, the orientated growth of the heteroid HKUST-1 on the BMZIF needs to overcome the mismatched cell lattices. First, the nanosized BMZIF dodecahedron core was prepared by a typical coordination approach, in which Zn^{2+} and Co^{2+} (Zn/Co molar ratio, 5/1) were used as metal nodes to coordinate with 2-methylimidazole. The BMZIF was added into a mixed solution of DMSO, $Cu(NO_3)_2$, and 1,3,5-H_3BTC to grow HKUST-1. To construct the core–shell HKZIF, instead of growing separately, reasonable control of the core/shell molar ratio and growth time is a crucial factor. Increasing the feed ratio of HKUST-1 gradually altered the corresponding composite colours from purple to aqua blue (Fig. 1(a)), indicating their successful recombination. Subsequently, the components in these composites were confirmed by powder X-ray diffraction (PXRD). Fig. 1(b) shows that the characteristic diffraction peaks of HKUST-1 began to appear at a core/shell molar ratio of 10/1; their peak intensities gradually increased as the ratios decreased, while it is opposite to the BMZIF. From 10 : 1 to 1 : 1, XRD patterns showed coexisting diffraction peaks for both MOFs that matched their simulation patterns well. N_2 sorption curves suggested the composite (using a 2/1 core/shell molar ratio) has combined the microporous features of the

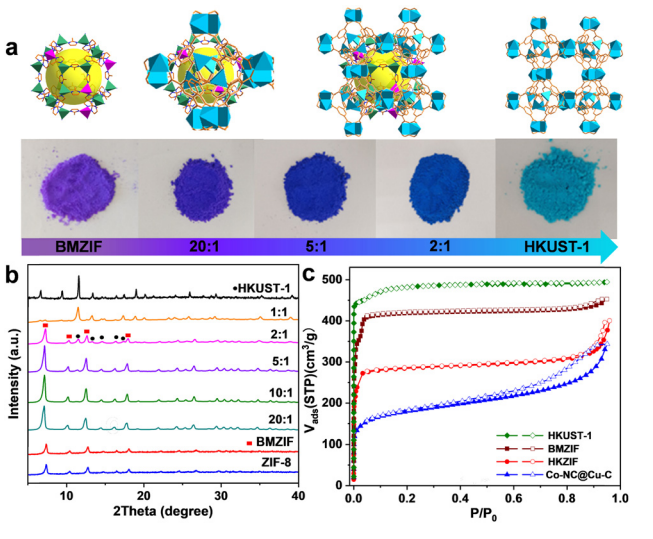

Fig. 1 (a) The sample color and the corresponding structure of the as-synthesized BMZIF, HKUST-1 and HKZIF. (b) PXRD patterns of a series of as-synthesized MOFs. (c) N_2 sorption isotherms of MOF precursors and Co–NC@Cu–C.

BMZIF and HKUST-1. BET surface areas for the BMZIF-5, HKUST-1, and HKZIF (2/1) were 1647.5, 1673.0 and 863.3 $m^2 g^{-1}$ (Fig. 1(c) and Fig. S1, ESI†), respectively. The decreased surface area of the HKZIF (2/1) was observed. We guess the partial pore windows of the BMZIF particle surface were covered and blocked by the growing HKUST-1.

A series of measurements confirmed the detailed BMZIF@HKUST-1 structure. The morphologies of the BMZIF and HKZIF (2 : 1) were measured by scanning electron microscopy (SEM). Fig. 2(a) shows BMZIF particles (150 nm) uniformly dispersed with well-defined dodecahedron morphology. After coating HKUST-1, the core–shell HKZIF particle retains a regular dodecahedron morphology and a size of ~200 nm (Fig. 2(b)). The detailed structure of the hybrid was further analyzed by transmission electron microscopy (TEM), elemental mapping and other measurements. The TEM image shows the dispersed core–shell NPs with the dark BMZIF core and gray HKUST-1 shell in each particle (Fig. 2(c)). The enlarged TEM image of one HKZIF particle clearly shows the core–shell structure and regular dodecahedron shape. The high-angle annular dark field scanning transmission electron microscopy (HAADF-STEM) image of the HKZIF in Fig. 2(d) confirmed the regular morphology. Elemental mappings of Zn, Co, and Cu verify their uniform dodecahedral distribution throughout the carbon skeleton (Fig. 2(e)–(g) and Fig. S2, ESI†). In addition, the smaller distribution area of Zn and Co relative to Cu illustrates that Zn and Co concentrate at the centre and Cu species distribute mainly on the outside of the particle. The HAADF-STEM image in Fig. 2(d) and the corresponding line-scan data confirm this structure assessment (Fig. 2(i)). These results clearly prove the well-directed growth of HKUST-1 on the BMZIF and successful synthesis of the core–shell HKZIF. Actually, there is some difficulty for the successful assembly of HKUST-1 and the BMZIF. We also attempted to grow the BMZIF on HKUST-1, but it failed. This was because the HKUST-1 surface was easily etched by alkalescent 2-methylimidazole. In addition, the growth time of HKUST-1 on the BMZIF was also one tricky point and affected greatly the final morphology of the HKZIF. When the core/shell molar ratio was 2/1, the optimal growth time was 10 min (Fig. S3, ESI†). There is not enough time for coordinative growth of HKUST-1 on the ZIF in a short time (5 min), while it would spontaneously nucleate and grow individual HKUST-1 particles when the time was extended (≥20 min).

Subsequently, the HKZIF precursor underwent pyrolysis under a 20% H_2/Ar atmosphere. During pyrolysis, the metal centers (Zn(II), Cu(II) and Co(II)) are reduced to their corresponding zero-valent states. Zn species readily evaporated along with the carrier gas due to its low boiling point. As a result, the BMZIF core produced Co encapsulated by porous N-doped C (named Co@NC) and the HKUST-1 shell converted into porous Cu@C. Their powder X-ray diffraction peaks are shown in Fig. 3(a). The diffraction peaks at ~44.21°, 51.52°, and 75.85° were assigned to metallic Co (JCPDS no. 15-0806), and the three peaks at around 43.29°, 50.43°, and 74.13° were indexed to metallic Cu (JCPDS no. 04-0836). No characteristic peak for the CoCu alloy was detected, which confirmed the successful generation of Co–NC@Cu–C NPs. The decreased surface areas and newly generated mesopores indicate the pore structure

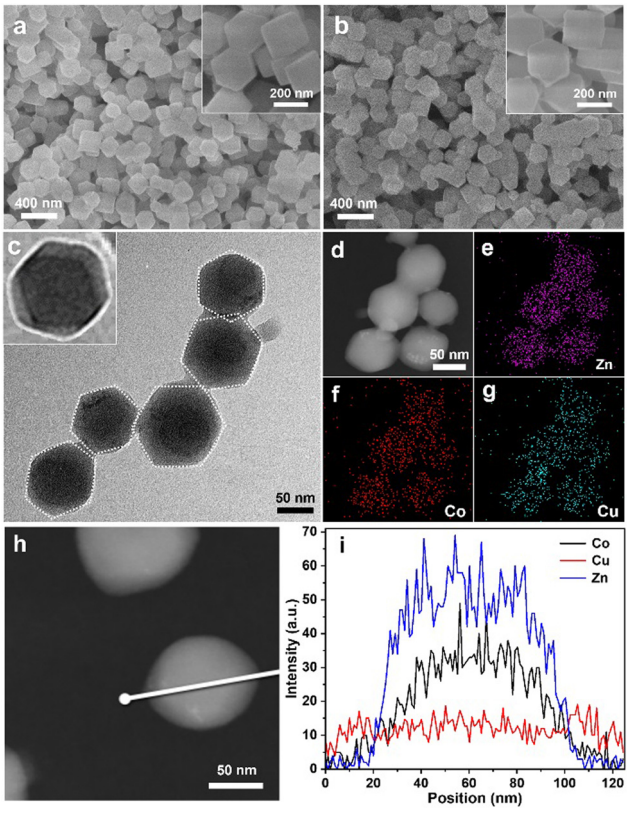

Fig. 2 SEM images of the (a) BMZIF and (b) HKZIF. (c) TEM image of the HKZIF. (d)–(g) HAADF-STEM images and the corresponding EDS elemental (Zn, Co, Cu) mapping of the HKZIF. (h) and (i) Line scanning spectra of the HKZIF.

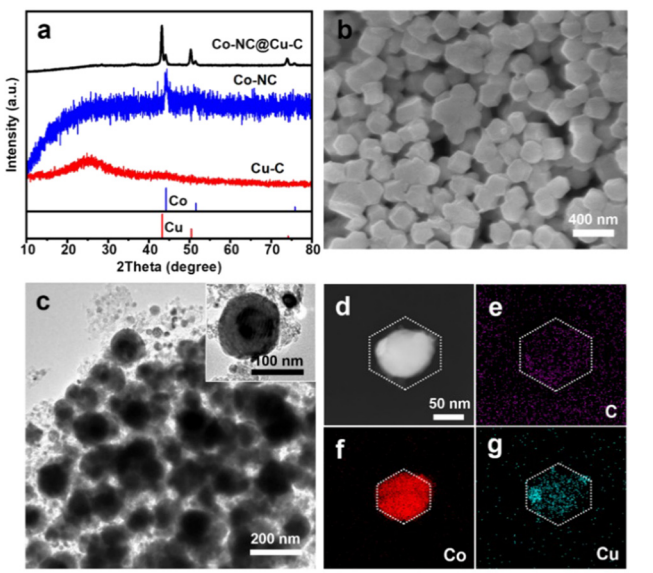

Fig. 3 (a) PXRD patterns of Cu–C, Co–NC, and Co–NC@Cu–C. (b) SEM, (c) TEM, and (d)–(g) HAADF-STEM images as well as the corresponding EDS elemental (C, Co, Cu) mapping of Co–NC@Cu–C.

transformation (Fig. 1(c) and Fig. S1, ESI†). The SEM images (Fig. 3(b)) show that Co–NC@Cu–C particles were well dispersed and retained the sizes and morphologies of their precursors. From the TEM images, most Co–NC@Cu–C particles retained the core–shell structure with the black core and dark shell (Fig. 3(c)). Generally, Co tends to have a deeper defocus contrast compared with Cu in TEM. The corresponding elemental mapping of C, Co, and Cu showed that the C element uniformly dispersed throughout the particle, Co species occupied the central position, and the Cu element distributed over a wider area with a darker centre than Co (Fig. 3(d)–(g)). These results further demonstrate the formation of the HKZIF and its successful transition to Co–NC@Cu–C.

X-ray photoelectron spectroscopy (XPS) characterization further confirmed the forms of Co and Cu in the samples. The Co 2p spectrum presents three forms of Co species at 778.35, 780.35 and 782.1 eV; these were metallic Co, Co_xO_y or CoC_xN_y, and Co–N_x, respectively (Fig. S4a, ESI†). The Cu 2p peaks at 934.2 eV and 932.7 eV were attributed to divalent Cu and zero-valent Cu, respectively (Fig. S4b, ESI†). Cu(0) species were oxidized readily to generate dissociative Cu(II) ions in most oxidation reactions, especially using coordinating solvents (*e.g.*, acetonitrile). Therefore, some changes should be made to avoid oxidation and prolong the lifetimes of Cu-based catalysts. Ion exchange by a spontaneous oxidation–reduction reaction effectively replaces a metal with another metal in solution. The standard reduction potentials of the Co/Co^{2+} (−0.28 V *vs.* the standard hydrogen electrode, SHE) and Cu/Cu^{2+} (0.34 V *vs.* SHE) pairs are much lower than those of noble metals, such as the Ag^+/Ag pair (0.799 V *vs.* SHE), Pd^{2+}/Pd pair (0.8 V *vs.* SHE) and the Pt^{2+}/Pt pair (1.2 V *vs.* SHE). Therefore, Cu species in Co–NC@Cu–C can be oxidized or replaced by the noble metal ions (Ag^+, Pt^{2+}, Pd^{2+}) (Fig. 4(a)). The solution colour changed during this replacement, which preliminarily confirmed successful ion exchange (Fig. 4(b)). For Co–NC@Cu–C, the solution colour gradually turned from blue to pink with increasing Ag^+ content, indicating that the copper shell is replaced first and then the cobalt core by Ag^+. Differently, the solution colour remained unchanged when adding $PtCl_6^{2-}$ or $PdCl_4^{2-}$ into the Cu–C sample, indicating no dissociative Cu^{2+} was released. According to the XRD analysis in Fig. 4(c), the emerging characteristic peaks of Ag and decreased peak intensity of Cu compared with those of Co–NC@Cu–C confirm the partial substitution of Cu by Ag. The surface valence state of various elements in Co–NC@CuAg–C was analyzed using XPS (Fig. S5, ESI†). The Cu $2p_{3/2}$ peaks of both divalent Cu and zero-valent Cu remained unchanged (Fig. S5a, ESI†). The sample displayed two obvious peaks centred at 368.33 and 374.33 eV, which corresponded to metallic Ag (Fig. S5b, ESI†).

Different from the commutative product by Ag^+, Cu(0) was mainly oxidized to Cu_2O by Pt^{2+}, *i.e.*, to Cu_2O at low Pd^{2+} content and CuO at high Pd^{2+} content (Fig. 4(c) and Fig. S6, ESI†). As the amount of Pd^{2+} increased, the peak intensities of Cu_2O gradually decreased until they disappeared. Finally, only the characteristic peaks of CuO were observed when using 10 wt% Pd. This is the same as that observed for Cu@C derived from HKUST-1: the Cu NPs were oxidized and transformed completely to CuO by 10 wt% Pd (Fig. S6, ESI†). Very weak diffractions of Pt or Pd species are detected from powder XRD patterns, presumably due to their low concentrations or small sizes. The presence of Pd(0) can be demonstrated from the XPS spectrum of Co–NC@CuOPd–C. The Pd 3d spectrum shows two signals of Pd $3d_{5/2}$ and Pd $3d_{3/2}$ electrons at 336.53 eV and 342.25 eV (Fig. S7, ESI†). The Cu 2p XPS spectrum shows two main signals of Cu $2p_{3/2}$ and Cu $2p_{1/2}$ at 934.2 eV and 954.3 eV, respectively (Fig. S7, ESI†), demonstrating that Cu0 was oxidized completely to CuO by Pd^{2+}. Fig. S8 (ESI†) shows the XPS spectral comparison of the Co 2p of Co–NC and Co–NC@CuOPd–C. It is worth noting that the Co 3d peaks in Co–NC@CuPd–C shifted to higher binding energies by ∼1.22 eV compared to Co–NC. The obvious blue shift of Co 3d suggested the existence of an interaction between the Co surface at the core–shell interface and the shell layer CuOPd–C. The elemental mapping in Fig. 4(d) confirmed the existence of C, Co, Cu, and Ag elements. Ag disperses primarily at the edges of the particle like hollow NPs, while the externally distributed Cu decreased declined due to their exchange. The actual amounts of Ag, Pd, and Pt in the Co–NC@CuAg–C, Co–NC@CuOPd–C and Co–NC@Cu_2OPt–C samples were measured by inductively coupled plasma atomic emission spectrometry (ICP-AES). The weight percentages (wt%) of Ag, Pd, and Pt were lower than their nominal values (Table S1, ESI†).

The performance of Co–NC@Cu–C and Co–NC@CuM (M = Ag, Pt, Pd)–C towards epoxidation of styrene employing O_2 as the oxidant, isobutyraldehyde as the co-catalyst and acetonitrile as the solvent was investigated. Table 1 shows a comparison of various catalysts for styrene oxidation. Co–NC@Cu–C had an 84.7% conversion with a selectivity of 81.8% to styrene oxide within 2 h at 80 °C (entry 1). For comparison, the CoCu-ZIF was synthesized and then pyrolyzed to give CoCu alloy NPs stabilized by N-doped C. The lattice fringe with an interplanar spacing of 0.207 nm in the high resolution transmission electron microscopy (HRTEM) image

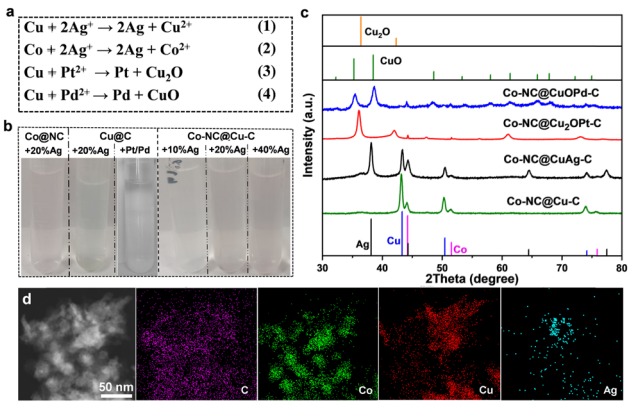

Fig. 4 (a) Ion exchange reactions. (b) Solution color changes during exchange using a series of catalysts. (c) PXRD patterns of Co–NC@CuM (M = Ag, Pt, Pd)–C. (d) HAADF-STEM images and the corresponding EDS elemental (C, Co, Cu, Ag) mapping of Co–NC@CuAg–C.

Table 1 Catalytic performance comparison of different catalysts in epoxidation of styrene[a]

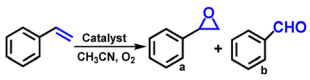

Entry	Catalyst	Time	T (°C)	Conv. (%)	Select. of a (%)
1	Co–NC@Cu–C	2 h	80	84.7	81.8
2	CoCu@NC	2 h	80	58.0	74.5
3	Cu@Ag@C(20%)	2 h	80	66.0	79.8
4	Co–NC@CuAg(20%)–C	2 h	80	94.0	81.5
5	Co–NC@Cu_2OPt(10%)–C	2 h	80	94.3	71.6
6	Co–NC@CuOPd(10%)–C	2 h	80	95.0	87.0
7	Co–NC	2 h	80	41.0	72.0
8	Cu–C	2 h	80	53.5	73.1
9[b]	Co–NC@Cu_2OPt(10%)–C	30 min	47	>99.0	94.5
10[b]	Co–NC@CuOPd(10%)–C	30 min	42	99.0	92.9
11[b]	Co–NC@Cu–C	30 min	53	52.3	49.4
12[b]	Co–NC	30 min	45	15.5	20.0
13[b]	Cu–C	30 min	46	21.6	25.2

[a] Reaction conditions: catalyst (20 mg), acetonitrile (10 mL), styrene (1.1 mmol), isobutyraldehyde (2.5 mmol), O_2 bubbling. [b] Reaction conditions: catalyst (20 mg), acetonitrile (10 mL), styrene (0.1 mmol), isobutyraldehyde (2 mmol), O_2 bubbling, visible light ($\lambda \geq 420$ nm).

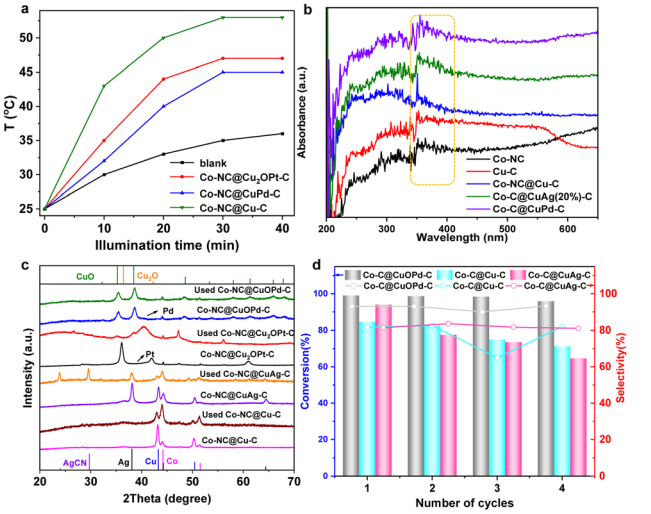

Fig. 5 (a) Photothermal conversion efficiency based on different materials. (b) UV-Vis absorption spectra of Co–NC, Cu–C, Co–NC@Cu–C and Co–NC@CuM–C. (c) XRD patterns of the catalysts Co–NC@Cu–C and Co–NC@CuM–C before and after the reaction. (d) Recyclability of Co–NC@CuOPd(10%)–C, Co–NC@Cu–C, and Co–NC@CuAg(20%)–C for styrene epoxidation.

was assigned to the (111) plane of CuCo alloy (Fig. S9, ESI†). The CoCu@NC presented relatively low conversion (58%) with a 74.5% selectivity of styrene epoxide under the same reaction conditions (entry 2). The result proved the advantage of constructing multilayer MOF structures. However, the solution colour after the above two reactions turned blue (Fig. S10, ESI†), which meant that most Cu was oxidized to Cu(II) by O_2, then dissolved upon coordination to acetonitrile. Although Co–NC@CuAg(20%)–C had a higher conversion (94.0%) and selectivity (81.5%) (entry 4), the light blue solution after the reaction was also observed (Fig. S10, ESI†). Silver also readily coordinates with acetonitrile and cannot protect copper from leaching. The Co–NC@Cu_2OPt(10%)–C had a conversion of 94.3% and a 71.6% selectivity (entry 5). However, the blue solution after the reaction indicated the dissolution of Cu_2O in acetonitrile. Interestingly, the nearly colourless solution after catalysis for Co–NC@CuOPd-(10%)–C confirmed the good stability of CuO in acetonitrile solvent (Fig. S10, ESI†). Introducing a small amount of Pd not only stabilized Cu, but increased the reaction conversion (95.0%) and SO selectivity (87.0%) (entry 6). For comparison, monometallic Co–NC and Cu–C had poor yields due to their few metal active sites (entries 7 and 8).

Interestingly, we found the photothermal effects of these carbon samples. Fig. 5(a) shows the photothermal conversion efficiencies of Co–NC@Cu_2OPt(10%)–C and Co–NC@CuOPd-(10%)–C under visible light irradiation. The solution temperature went up approximately to 45–55 °C upon the Co–NC@CuPd–C, Co–NC@Cu_2OPt–C and Co–NC@Cu–C. This can be explained by their good light absorption ability. According to UV-Vis diffuse reflectance spectra, all the samples have a visible light absorption band at 330–400 nm (Fig. 5(b)). Therefore, the epoxidation of styrene was further investigated using visible light instead of external heating. The Co–NC@CuOPd–C exhibited high activity (>99% conversion in 30 min) and selectivity (92.9%). Co–NC@Cu_2OPt–C also had excellent activity and SO selectivity compared with monometallic Co–NC and Cu–C (entries 9–13). Their catalytic performance exceeded most reported catalysts for styrene epoxidation (Table S2, ESI†). The PXRD patterns of Co–NC@Cu–C and Co–NC@CuM–C (M = Ag, Pt, Pd) catalysts before and after the reaction are shown in Fig. 5(c). According to the data, the diffraction peaks of Cu decreased clearly for the Co–NC@Cu–C catalyst after the reaction. The characteristic peaks of both Cu and Ag had a clear intensity decline, accompanied by the emerging peaks of AgCN for Co–NC@CuAg–C after the 1st run. This result combined with the blue solution confirmed our speculation that both Cu and Ag initially oxidized and coordinated with acetonitrile. Similarly, the strong peaks of Cu_2O almost disappeared for Co–NC@Cu_2OPt–C after the reaction, indicating the same instability of Cu_2O in acetonitrile. Interestingly, the diffraction peaks of used Co–NC@CuOPd–C remained virtually unchanged, which confirmed the superior stability of CuO. In addition, the ICP analysis of Co–NC@CuOPd–C after catalysis shown almost the same metal contents as those of fresh Co–NC@CuOPd–C (Table S1, ESI†). This result further demonstrated the stability of Co–NC@CuOPd–C. In order to investigate the mechanism of epoxidation of styrene, the quenchers of different reactive oxygen species ($^1O_2$, $^\bullet OH$, $^\bullet O_2^-$) were introduced into the reaction system. In the presence of sodium amide (NaN_3, quenching for $^1O_2$) and IPA (quenching for $^\bullet OH$), there was almost no obvious decrease in the conversion of styrene (Fig. S11, ESI†). No products were detected when adding superoxide dismutase (SOD), indicating that $^\bullet O_2^-$ has an important contribution to the epoxidation of styrene. According to the above experimental results and related literature,[67,68] a possible mechanism for the epoxidation of styrene with O_2 is proposed. As shown in Scheme S1a (ESI†), the CuOPd shell with abundant charge transferred electrons to O_2 to produce $^\bullet O_2^-$. The obtained $^\bullet O_2^-$ and isobutyryl radical combined with H^+ to generate isobutyl peroxyacid. The isobutyl peroxyacid produced finally reacted with styrene to form

styrene oxide. The oxidation pathway of benzaldehyde is shown in Scheme S1b (ESI†). The isobutyryl radical reacted with O_2 to produce an isobutylperoxy radical, which reacted with the olefinic bond of styrene to form a complex radical. Then the intermediate reacted with O_2 to generate a new radical intermediate, which further decomposed to give benzaldehyde.

Subsequently, the recyclability of several position exchanged samples was investigated under the same reaction conditions, which is a very significant practical consideration for large-scale applications. It is worth noting that the Co–NC@CuOPd–C catalyst can be reused at least four times without an obvious activity change (Fig. 5(d)). For comparison, the obvious activity decline during four reuse cycles for both Co–NC@CuAg–C and Co–NC@Cu–C was mainly due to the massive leaching of Cu and Ag species (Fig. 5(d)). Although all exchanged products (Cu, Cu_2O, CuO) have good catalytic activity, only CuO has the best stability under harsh reaction conditions. In addition, the alloyed Pd may protect the CuO from dissolution to some extent. The Co–NC@CuAg–C and Co–NC@Cu_2OPt–C may be suitable for other reaction conditions. Therefore, this ion exchange strategy provides a novel and effective method to prevent the leaching of Cu species under an oxidizing atmosphere.

3 Conclusions

In this work, we have successfully realized the directed epitaxial growth of hierarchical HKUST-1 on the BMZIF to obtain a novel trimetallic BMZIF@HKUST-1 heterostructure. During assembly, the regular morphology, size and composition of the hybrids were effectively controllable. After direct carbonization, the core–shell Co–NC@Cu–C material containing both Cu and Co active sites was successfully obtained. To stabilize Cu species in Co–NC@Cu–C for styrene epoxidation under harsh conditions, ion exchange with noble metal ions (M = Ag, Pt, Pd) was adopted. Among the exchanged products, Co–NC@CuOPd–C optimized the stability in catalytic styrene epoxidation by photothermal catalysis under moderate conditions. Moreover, the good SO yield with >90% selectivity exceeds those of most reported catalysts, even some noble metals. The excellent catalytic performance of Co–NC@CuOPd–C stems mainly from multiple active sites (Co, CuO, Pd), good stability, and its porous structure. This work provided a novel method to prevent Cu NPs in Cu-based catalysts from coordinative leaching. In addition, the design strategy of hierarchical core–shell MOFs would explore more active sites for the synthesis of various fine chemicals.

Conflicts of interest

There are no conflicts to declare.

Acknowledgements

This work was supported by the National Natural Science Foundation of China (22275108) and the Excellent Youth Foundation of Shandong Natural Science Foundation (ZR2020YQ08).

Notes and references

1 Y. Xiong, W. Sun, P. Xin, W. Chen, X. Zheng, W. Yan, L. Zheng, J. Dong, J. Zhang, D. Wang and Y. Li, *Adv. Mater.*, 2020, **32**, 2000896.
2 M. Li, L. Ma, L. Luo, Y. Liu, M. Xu, H. Zhou, Y. Wang, Z. Li, X. Kong and H. Duan, *Appl. Catal., B*, 2022, **309**, 121268.
3 H. Fu, K. Huang, G. Yang, Y. Cao, H. Wang, F. Peng, X. Cai, H. Gao, Y. Liao and H. Yu, *ACS Catal.*, 2021, **11**, 8872–8880.
4 K. Kamata, K. Yonehara, Y. Sumida, K. Yamaguchi, S. Hikichi and N. Mizuno, *Science*, 2003, **300**, 964–966.
5 D. Banerjee, R. V. Jagadeesh, K. Junge, M.-M. Pohl, J. Radnik, A. Bruckner and M. Beller, *Angew. Chem., Int. Ed.*, 2014, **53**, 4359–4363.
6 B. Jia, L. Bai, Z. Han, R. Li, G. Huangfu, C. Li, J. Zheng, Y. Qu, K. Leng, Y. Wang and J. Bai, *ACS Appl. Mater. Interfaces*, 2022, **14**, 10337–10343.
7 F. Zhang, X. Zhao, C. Feng, B. Li, T. Chen, W. Lu, X. Lei and S. Xu, *ACS Catal.*, 2011, **1**, 232–237.
8 S. Tian, B. Wang, W. Gong, Z. He, Q. Xu, W. Chen, Q. Zhang, Y. Zhu, J. Yang, Q. Fu, C. Chen, Y. Bu, L. Gu, X. Sun, H. Zhao, D. Wang and Y. Li, *Nat. Commun.*, 2021, **12**, 3181.
9 B. Liu, P. Wang, A. Lopes, L. Jin, W. Zhong, Y. Pei, S. L. Suib and J. He, *ACS Catal.*, 2017, **7**, 3483–3488.
10 J. Liu, R. Meng, J. Li, P. Jian, L. Wang and R. Jian, *Appl. Catal., B*, 2019, **254**, 214–222.
11 F. Li, J. Tang, Q. Ke, Y. Guo, M. N. Ha, C. Wan, Z. Lei, J. Gu, Q. Ling, V. N. Nguyen and W. Zhan, *ACS Catal.*, 2021, **11**, 11855–11866.
12 A. S. Shaarma, V. S. Sharma, H. Kaur and R. S. Varma, *Green Chem.*, 2020, **22**, 5902–5936.
13 J. Sebastian, K. M. Jinka and R. V. Jasra, *J. Catal.*, 2006, **244**, 208–218.
14 G. Xu, Q.-H. Xia, X.-H. Lu, Q. Zhang and H.-J. Zhan, *J. Mol. Catal. A: Chem.*, 2007, **266**, 180–187.
15 X. Chen, Y. Zou, M. Zhang, W. Gou, S. Zhang and Y. Qu, *J. Mater. Chem. A*, 2022, **10**, 6016.
16 B. Paul, S. K. Sharma, R. Khatun, S. Adak, G. Singh, V. Joshi, M. K. Poddar, A. Bordoloi, T. Sasaki and R. Bal, *Ind. Eng. Chem. Res.*, 2019, **58**, 18168–18177.
17 X. Li, X.-H. Zhu, Y. Fang, H.-L. Yang, X. Zhou, W. Chen, L. Jiao, H. Huo and R. Li, *J. Mater. Chem. A*, 2014, **2**, 10485–10491.
18 L. Wang, H. Wang, A. E. Rice, W. Zhang, X. Li, M. Chen, X. Meng, J. P. Lewis and F.-S. Xiao, *J. Phys. Chem. Lett.*, 2015, **6**, 2345–2349.
19 Y. Fu, L. Xu, H. Shen, H. Yang, F. Zhang, W. Zhu and M. Fan, *Chem. Eng. J.*, 2016, **299**, 135–141.
20 Y. Huang, Z. Liu, G. Gao, G. Xiao, A. Du, S. E. Bottle, S. Sarina and H. Zhu, *ACS Catal.*, 2017, **7**, 4975–4985.
21 M. R. Nabid, Y. Bide and M. Abuali, *RSC Adv.*, 2014, **4**, 35844.
22 Z. Wang and S. M. Cohen, *Chem. Soc. Rev.*, 2009, **38**, 1315–1329.
23 H. Furukawa, K. E. Cordova, M. O'Keeffe and O. M. Yaghi, *Science*, 2013, **341**, 1230444.

24 H. Zhou and S. Kitagawa, *Chem. Soc. Rev.*, 2014, **43**, 5415.
25 R.-B. Lin, L. Li, H.-L. Zhou, H. Wu, C. He, S. Li, R. Krishna, J. Li, W. Zhou and B. Chen, *Nat. Mater.*, 2018, **17**, 1128–1133.
26 Z. Lu, J. Duan, H. Tan, L. Du, X. Zhao, R. Wang, S. Kato and S. Yang, *J. Am. Chem. Soc.*, 2023, **145**, 4150–4157.
27 O. M. Yaghi and Z. Rong, *Science*, 2023, **379**, 330–331.
28 L. Jiao, J. Wang and H.-L. Jiang, *Acc. Mater. Res.*, 2021, **2**, 327–339.
29 H. Liu, W. Liu, G. Xue, T. Tan, C. Yang, P. An, W. Chen, W. Zhao, T. Fan, C. Cui, Z. Tang and G. Li, *J. Am. Chem. Soc.*, 2023, **145**, 11085–11096.
30 M. Zhao, K. Yuan, Y. Wang, G. Li, J. Guo, L. Gu, W. Hu, H. Zhao and Z. Tang, *Nature*, 2016, **539**, 76–80.
31 Q. Huang, Q. Niu, X.-F. Li, J. Liu, S.-N. Sun, L.-Z. Dong, S.-L. Li, Y.-P. Cai and Y.-Q. Lan, *Sci. Adv.*, 2022, **8**, eadd5598.
32 C.-C. Cao, C.-X. Chen, Z.-W. Wei, Q.-F. Qiu, N.-X. Zhu, Y.-Y. Xiong, J.-J. Jiang, D. Wang and C.-Y. Su, *J. Am. Chem. Soc.*, 2019, **141**, 2589–2593.
33 M. A. El-Bindary, M. G. El-Desouky and A. A. El-Bindary, *Appl. Organomet. Chem.*, 2022, **36**, e6660.
34 M. Ding, W. Liu and R. Gref, *Adv. Drug Delivery Rev.*, 2022, **190**, 114496.
35 H. Yuan, N. Li, W. Fan, H. Cai and D. Zhao, *Adv. Sci.*, 2022, **9**, 2104374.
36 W.-H. Deng, L. He, E.-X. Chen, G.-E. Wang, X.-L. Ye, Z.-H. Fu, Q. Lin and G. Xu, *J. Mater. Chem. A*, 2022, **10**, 12977.
37 M. A. Gaidimas, F. A. Son, M. R. Mian, T. Islamoglu and O. K. Farha, *ACS Appl. Mater. Interfaces*, 2022, **14**, 47222–47229.
38 Y. Ye, Y. Xie, Y. Shi, L. Gong, J. Phipps, A. M. Al-Enizi, A. Nafady, B. Chen and S. Ma, *Angew. Chem., Int. Ed.*, 2023, **62**, e202302564.
39 O. T. Qazvini and S. G. Telfer, *J. Mater. Chem. A*, 2020, **8**, 12028–12034.
40 X. Zhao, Y. Wang, D.-S. Li, X. Bu and P. Feng, *Adv. Mater.*, 2018, **30**, 1705189.
41 L. Yang, X. Zeng, W. Wang and D. Cao, *Adv. Funct. Mater.*, 2018, **28**, 1704537.
42 H.-L. Jiang, B. Liu, Y.-Q. Lan, K. Kuratani, T. Akita, H. Shioyama, F. Zong and Q. Xu, *J. Am. Chem. Soc.*, 2011, **133**, 11854–11857.
43 S.-N. Zhao, X.-Z. Song, S.-Y. Song and H.-J. Zhang, *Coord. Chem. Rev.*, 2017, **337**, 80–96.
44 X. Xie, L. Shang, X. Xiong, R. Shi and T. Zhang, *Adv. Energy Mater.*, 2022, **12**, 2102688.
45 Y. Zhou, B. Tang, S. Wang and J. Long, *Int. J. Hydrogen Energy*, 2020, **45**, 15785–15795.
46 H.-Q. Yin, Z.-M. Zhang and T.-B. Lu, *Acc. Chem. Res.*, 2023, **56**, 2676–2687.
47 J. Li, Y. Chen, Y. Tang, S. Li, H. Dong, K. Li, M. Han, Y.-Q. Lan, J. Bao and Z. Dai, *J. Mater. Chem. A*, 2014, **2**, 6316.
48 L. Hu, W. Li, L. Wang and B. Wang, *EnergyChem*, 2021, **3**, 100056.
49 J. Gao, Q. Huang, Y. Wu, Y.-Q. Lan and B. Chen, *Adv. Energy Sustainability Res.*, 2021, **2**, 2100033.
50 Y. Gu, Y. Wu, L.-N. Li, W. Chen, F. Li and S. Kitagawa, *Angew. Chem., Int. Ed.*, 2017, **56**, 15658–15662.
51 S. Choi, T. Kim, H. Ji, H. J. Lee and M. Oh, *J. Am. Chem. Soc.*, 2016, **138**, 14434–14440.
52 X.-G. Wang, L. Xu, M.-J. Li and X.-Z. Zhang, *Angew. Chem., Int. Ed.*, 2020, **59**, 18078–18086.
53 T. Li, J. E. Sullivan and N. L. Rosi, *J. Am. Chem. Soc.*, 2013, **135**, 9984–9987.
54 J. Yang, F. Zhang, H. Lu, X. Hong, H. Jiang, Y. Wu and Y. Li, *Angew. Chem., Int. Ed.*, 2015, **54**, 10889–10893.
55 G. Lee, S. Lee, S. Oh, D. Kim and M. Oh, *J. Am. Chem. Soc.*, 2020, **142**, 3042–3049.
56 Y. Gong, Y. Yuan, C. Chen, P. Zhang, J. Wang, A. Khan, S. Zhuiykov, S. Chaemchuen and F. Verpoort, *J. Catal.*, 2019, **375**, 371–379.
57 S. Furukawa, K. Hirai, K. Nakagawa, Y. Takashima, R. Matsuda, T. Tsuruoka, M. Kondo, R. Haruki, D. Tanaka, H. Hirotoshi Sakamoto, S. Shimomura, O. Sakata and S. Kitagawa, *Angew. Chem., Int. Ed.*, 2009, **48**, 1766–1770.
58 M.-S. Yao, J.-W. Xiu, Q.-Q. Huang, W.-H. Li, W.-W. Wu, A.-Q. Wu, L.-A. Cao, W.-H. Deng, G.-E. Wang and G. Xu, *Angew. Chem., Int. Ed.*, 2019, **58**, 14915–14919.
59 W. Liu, J. Huang, Q. Yang, S. Wang, X. Sun, W. Zhang, J. Liu and F. Huo, *Angew. Chem., Int. Ed.*, 2017, **56**, 5512–5516.
60 S. Choi, T. Kim, H. Ji, H.-J. Lee and M. Oh, *J. Am. Chem. Soc.*, 2016, **138**, 14434–14440.
61 J. Zhuang, L.-Y. Chou, B. T. Sneed, Y. Cao, P. Hu, L. Feng and C.-K. Tsung, *Small*, 2015, **11**, 5551–5555.
62 M. Zhao, J. Chen, B. Chen, X. Zhang, Z. Shi, Z. Liu, Q. Ma, Y. Peng, C. Tan, X.-J. Wu and H. Zhang, *J. Am. Chem. Soc.*, 2020, **142**, 8953–8961.
63 C. Liu, Q. Sun, L. Lin, J. Wang, C. Zhang, C. Xia, T. Bao, J. Wan, R. Huang, J. Zou and C. Yu, *Nat. Commun.*, 2020, **11**, 4971.
64 H. J. Lee, Y. J. Cho, W. Cho and M. Oh, *ACS Nano.*, 2013, **7**, 491–499.
65 H. Guo, A. Che, W. Mi, Y. Zhang and X. Shi, *J. Mater. Chem. A*, 2023, **11**, 19145–19152.
66 Y.-Z. Chen, C. Wang, Z.-Y. Wu, Y. Xiong, Q. Xu, S.-H. Yu and H.-L. Jiang, *Adv. Mater.*, 2015, **27**, 5010–5016.
67 Q. Yue, Y. Lu, Z. Zhang, H. Tian, H. Wang, X. Li and S. Liu, *New J. Chem.*, 2020, **44**, 16913–16920.
68 B.-B. Wentzel, P.-A. Gosling, M.-C. Feiters and R. J. M. Nolte, *J. Chem. Soc., Dalton Trans.*, 1998, 2241–2246.